SCIEPublish

Article

SnS_2 Quantum Dots Decorated MoS_2 Nanosheets Enabling Efficient Photocatalytic H_2 Evolution in CO_2 Saturated Water

Xuelian Chen [1,2], Xi Luo [1], Lei Liu [3], Jing Ping [1] and Songmei Sun [1,4,*]

[1] Textile Pollution Controlling Engineering Center of Ministry of Environmental Protection, College of Environmental Science and Engineering, Donghua University, Shanghai 201620, China; xuelianchen_ncie@163.com (X.C.); xuelianchen_ncie@163.com (X.L.); 1625731825@qq.com (J.P.)

[2] Shenhua (Beijing) New Materials Technology CO. LTD, CHN Energy Group, Beijing 102211, China

[3] Center for Advanced Low-Dimension Materials, Donghua University, Shanghai 201620, China; liulei@dhu.edu.cn (L.L.)

[4] Shanghai Institute of Pollution Control and Ecological Security, 1239 Siping Road, Shanghai 200092, China

* Corresponding author. sunsm@dhu.edu.cn (S.S.)

Received: 13 December 2022; Accepted: 1 March 2023; Available online: 3 March 2023

ABSTRACT: SnS_2/MoS_2 heterojunction nanocomposite was prepared by a one-step hydrothermal synthesis method. The nanocomposite exhibited much improved photocatalytic hydrogen evolution performance in CO_2 saturated solution compared with pure MoS_2 and SnS_2 samples. The improved photocatalytic activity was attributed to the S-scheme heterojunction structure between SnS_2 quantum dots and MoS_2 nanosheets which facilitate electron-hole separation both in MoS_2 and SnS_2. In the S-scheme structure, the strong reduction ability of SnS_2 quantum dots was well maintained for the improved H_2 evolution. In situ DRIFT studies allowed us to suggest reaction pathways from CO_2 and H_2O to photocatalytic H_2, CO, and CH_4 generation.

Keywords: Photocatalysis; H_2 evolution; CO_2 hydrogenation; S-scheme

1. Introduction

The majority of global energy consumption is mainly supplied by fossil fuels combustion currently, which inevitably causes environmental problems and energy shortage, thus stimulating scientists for seeking renewable and green energy sources. Photocatalytic hydrogen evolution from water is a significant reaction for using renewable energy, which needs highly efficient and stable catalysts. During the past decades, various studies have been devoted to exploring highly efficient photocatalysts for H_2 evolution from water, including metal oxides [1–3], metal chalcogenides [4], and some other semiconductors [5].

Although great achievements have been made in the development of H_2 evolution photocatalysts, there are still several challenges to its practical application. One of the main bottlenecks is the severe charge carrier recombination of the photogenerated electron-hole pairs during their transfer process [6]. Designing a heterojunction structure is widely used to improve the electron-hole separation and suppress the recombination behavior of charge carriers [7]. Recently, a new step-scheme (S-scheme) heterojunction with a staggered band structure has been proposed [8], which is composed of two n-type semiconductor photocatalysts for reduction and oxidation reactions, respectively. In the S-scheme heterojunction, the electrons in the oxidation photocatalyst and the holes in the reduction photocatalyst will recombine in the interface, leaving the more powerful photogenerated electrons in the conduction band (CB) of the reduction photocatalyst, and the more powerful photogenerated holes in the valence band (VB) of oxidation photocatalyst, respectively. Therefore, the charge transfer route in this system makes the heterojunction has a strong redox ability. Due to these advantages, photocatalysts with the S-scheme structure have been utilized in many fields, such as water splitting [7–12], pollutant degradation [13–18], CO_2 photoreduction [19–28], and inactivation of bacteria [29–32]. These investigations indicate that the construction of S-scheme heterojunction can be an ideal option to design high-performance photocatalysts.

Among various photocatalysts, metal sulfides have attracted widespread attention in recent years [33,34]. Especially, molybdenum disulfide (MoS_2), as a typical transition metal sulfide, has been considered as a promising hydrogen evolution reaction (HER) catalyst because of its low energy barriers for hydrogen adsorption and desorption. MoS_2 has a layer-dependent band gap; for bulk the value is 1.2 eV and it increases to 1.9 eV for monolayer [34], which is suitable for visible light-driven photocatalysis.

However, bare MoS_2 usually has poor photocatalytic HER activity from pure water splitting because of its relatively low conduction band potential −0.16 eV [35,36], which is not sufficient for H^+ reduction to produce H_2 (−0.41 V vs. NHE at pH 7). SnS_2, an inexpensive and nontoxic semiconductor with a band gap of 2.0–2.25 eV [4,37], has recently been proven to be a relatively stable and efficient visible-light-driven photocatalyst which has a higher conduction band edge position than that of MoS_2 [38]. Nevertheless, the practical applications of single SnS_2 have also been limited by the high electron-hole recombination rate and the inferior charge transfer rate [39]. Up to the present, considerable research efforts have been devoted to exploring S-scheme heterojunction with SnS_2 and MoS_2 for their photocatalytic applications, such as MoS_2/SnS_2/r-GO for CO_2 reduction [40], 2D/2D SnS_2/MoS_2 nanosheets for methylene blue decomposition [41] and CNT@MoS_2/SnS_2 nanostructure for efficient Cr(VI) reduction [42]. These studies proved the existence of S-scheme heterojunction between SnS_2 and MoS_2 semiconductors because of their increased electron-hole separation and improved photocatalytic activities in heterojunction structure. However, besides the photocatalytic activity, selectivity is another important factor that influences the performance of a photocatalyst, which has rarely been studied in S-scheme heterojunction photocatalysts. Previous studies have shown that accumulated electrons on the catalyst surface facilitate multi-electron reduction reactions, meanwhile dispersed electrons are inclined to participate in single or two electron reduction processes [43–46]. In an S-scheme MoS_2/SnS_2 heterojunction structure, photo-excited electrons in the CB of MoS_2 will combine with holes in the VB of SnS_2 owing to internal electric field (IEF), leaving the CB electrons of SnS_2 and VB holes of MoS_2 highly dispersed on the heterojunction surface. From this viewpoint, we can use this type of MoS_2/SnS_2 heterostructure to improve the selectivity of single or two electron reduction reactions, such as H_2 evolution from CO_2 saturated water. Furthermore, previous studies have demonstrated that the quantum-sized photocatalyst is more advantageous in photocatalysis when compared with the larger nanoscale photocatalyst, because of its increased redox potentials of photogenerated electrons and holes by quantum confinement effect [47].

Inspired by the afore-mentioned unique features, we adopted a one-step in situ synthesis method, to design a 0D/2D S-scheme heterojunction involving MoS_2 nanosheets decorated with SnS_2 quantum dots (QDs) for H_2 evolution in CO_2 saturated water solution. A series of analytical techniques including XPS, TEM, XRD, and UV-vis diffuse reflectance measurements have been utilized to study morphology, structural and optical properties of photocatalysts. The photocatalytic efficiency is measured by H_2 evolution in CO_2 saturated water upon Xenon light irradiation. It was found the SnS_2/MoS_2 S-scheme heterojunction can significantly improve H_2 evolution performance. The H_2 evolution rate of SnS_2/MoS_2, SnS_2 and MoS_2 are 42.49, 22.09, and 11.19 $\mu mol \cdot g^{-1} \cdot h^{-1}$, respectively, in CO_2 saturated pure water under the conditions we used. Moreover, in-situ diffuse reflectance infrared Fourier transform spectroscopy (DRIFTS) was applied to explore the reaction pathways. A mechanism is proposed based on these characterizations.

2. Experimental Section

2.1. Preparations

All reagents were of analytical grade and were used as received without further purification.

For preparation of pure MoS_2 sample, 30 mmol thiourea was dissolved in 70 mL deionized water under vigorous stirring. After that, 5 mmol sodium molybdate dehydrate ($Na_2MoO_4 \cdot 2H_2O$) was added and then stirred for 0.5 h to form a homogeneous solution. The solution was then transferred into a 100 mL Teflon-lined stainless steel autoclave up to 70% of the total volume. The autoclave was heated at 220 °C for 18 h at autogenous pressure, and then cooled to room temperature naturally. The resulting sample was separated by centrifugation from the reaction solution and washed with deionized water and absolute alcohol several times. The obtained solid MoS_2 slurry were dispersed in water and sonicated for 1 h to form a MoS_2 suspension, which was then freeze-dried for further characterization.

For the SnS_2 nanosheet sample, 15 mmol thiourea was dissolved in 70 mL deionized water under magnetic stirring for 0.5 h to form a transparent solution. 2.5 mmol $SnCl_4 \cdot 5H_2O$ was added to the solution followed by stirring 0.5 h to form a transparent precursor solution. The precursor suspension was then transferred to 100 mL Teflon-lined stainless-steel autoclave, maintained at 220 °C for 18 h. After that, the reactor was cooled down to room temperature naturally for about 12 h. Then, the solid product was collected by centrifugation and washed by ethanol and distilled water several times, and then freeze-dried for further characterization.

For preparation of the SnS_2/MoS_2 nanocomposite, 30 mmol thiourea was dissolved in 70 mL deionized water under vigorous stirring. After that, 2.5 mmol $Na_2MoO_4 \cdot 2H_2O$ and 2.5 mmol $SnCl_4 \cdot 5H_2O$ were added and stirred for 0.5 h to form a homogeneous solution. This solution was transferred into a 100 mL Teflon-lined stainless steel autoclave up to 70% of the total volume. The autoclave was heated to 220 °C and maintained at 220 °C for 18 h. After that, the reactor was cooled down to room temperature naturally. The obtained SnS_2/MoS_2 solid product was separated by centrifugation from the reaction solution, washed with absolute ethanol and deionized water several times, and then freeze-dried for further characterization.

2.2. Characterizations

The crystal structures were characterized through powder XRD patterns, which were obtained using a Japan Rigaku X-ray diffractmeter/RINT2500HLR+ with Cu Kα radiation operating at 40 kV and 80 mA (Rigaku, Tokyo, Japan). The transmission electron microscope (TEM) analyses were carried out using a JEOL JEM-2100F field emission electron microscope (JEOL, Tokyo, Japan). X-ray photoelectron spectroscopy (XPS) spectra were collected using a PHI5000VersaProbe spectrometer (ULVAC PHI, Chigasaki, Japan). UV-vis absorption spectra of the samples were measured by a Shimadzu UV-3600 Spectrophotometer (Shimadzu, Kyoto, Japan). The in-situ DRIFT measurement was performed on a Nicolet 8700 DRIFT spectrometer using KBr window (Thermo Fisher Scientific, Waltham, MA, USA).

2.3. Photocatalytic Test

Photocatalytic H_2 evolution in CO_2 saturated water was performed under a 300 W Xenon light (full spectrum) at atmospheric pressure. Typically, a total of 0.025 g catalyst was added to a homemade quartz reactor (600 cm^3), which was located approximately 10 cm from the lamp. 50 mL of deionized water was injected into the reactor and sonicated for 0.5 h for the dispersion of the catalyst. After that, pure CO_2 (99.99%) was slowly bubbled through the reactor for 20 min to remove the air in the reactor. Then the reactor was sealed and irradiated under Xenon light for various times. During the experiment, the temperature of the reactor was maintained at 15 °C by providing a flow of cooling water. All products were quantified by gas chromatography (GC) equipped with a thermal conductivity detector and flame ionization detector.

2.4. Electrochemical Measurements

Electrochemical measurements were performed on a CHI 700E electrochemical workstation using a standard three-electrode cell. The working electrodes were prepared from the photocatalysts. A platinum mesh and a standard saturated calomel electrode (SCE) were used as a counter electrode and a reference electrode, respectively. To prepare the working electrodes, 5 mg of the photocatalyst was added into 0.1 mL of 1% Nafion solution in ethanol and sonicated for 1 min. After that, the obtained slurry was dispersed onto a 2 cm × 1.5 cm FTO glass by dip coating and dried at 25 °C.

3. Results and Discussion

3.1. Catalyst Characterizations

The crystal structures of MoS_2, SnS_2, and SnS_2/MoS_2 composites were analyzed by XRD, as shown in Figure 1. The XRD pattern of the as-synthesized MoS_2 sample can be indexed to the hexagonal structure of MoS_2 (JCPDS No. 75-1539). For the as-prepared MoS_2, the detected peaks at 2θ = 14.1°, 32.9°, 39.5°, 49.4°, and 58.7° are assigned to the (002), (100), (103), (105), and (110) planes of the hexagonal phase. The diffraction peaks of SnS_2 located at 2θ = 15.0°, 28.3°, 32.2°, 41.9°, 50.1°, and 52.6° can be indexed to (001), (100), (011), (012), (110), and (111) planes of hexagonal SnS_2 (JCPDS No.83-1705). Both the diffraction peaks of SnS_2 and MoS_2 can be observed in the case of SnS_2/MoS_2 composite materials. Besides that, an additional peak at 26.2° is observed in the XRD pattern of SnS_2/MoS_2, which can be indexed to a tiny amount of SnO in the interface of SnS_2/MoS_2. The formation of SnO is inevitable during the preparation of SnS_2/MoS_2 heterojunction. When SnS_2 closely contacted with MoS_2, the electrons in SnS_2 would flow to MoS_2 spontaneously to maintain Fermi energy at the same level. After that, the surface adsorbed O_2 molecules would donate electrons to SnS_2 and lead to the formation of tiny SnO species.

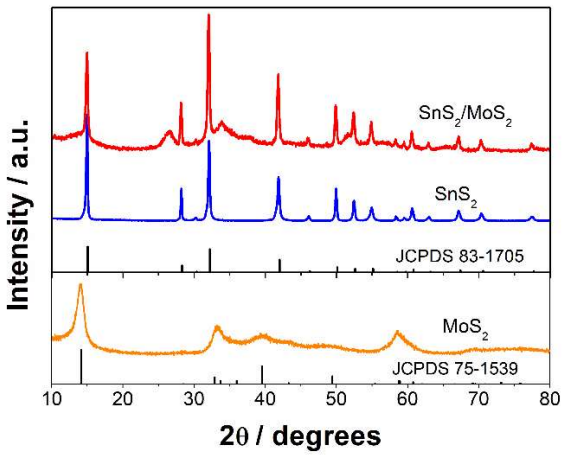

Figure 1. XRD patterns of MoS_2, SnS_2 and SnS_2/MoS_2.

The detailed morphology of the as-prepared catalysts was further determined by transmission electron microscopy (TEM) measurement. Figure 2a shows the low-magnified TEM image of the as-prepared MoS_2. Figure 2b is the low-magnified TEM image of the hydrothermally synthesized SnS_2. Hexagonal nanosheets with an average size of 200~500 nm can be observed in Figure 2b. The selected area electron diffraction (SAED) from one single SnS_2 hexagonal nanosheet is shown in Figure 2c, which indicates the single crystallinity of the as-prepared SnS_2. This is further confirmed from its high-resolution TEM image in Figure 2d. As shown in Figure 2d, two lattice distances of 0.32 nm are observed from (010) and (100) planes of hexagonal SnS_2, indicating that the surface plane of hexagonal SnS_2 is (001) plane. Figure 2e shows the low-magnified TEM image of the SnS_2/MoS_2 nanocomposite, which indicates a quantum dot decorated sheet like structure. The particle size of SnS_2 quantum dot in the nanocomposite is about 4~7 nm. The average thickness of the MoS_2 nanosheet in the nanocomposite is 3~10 nm. From the TEM image, it is obvious that the composite structure restricted the crystal growth of SnS_2. HRTEM image of the SnS_2/MoS_2 nanocomposite in Figure 2f further confirmed the quantum dots decorated sheet-like nanostructure.

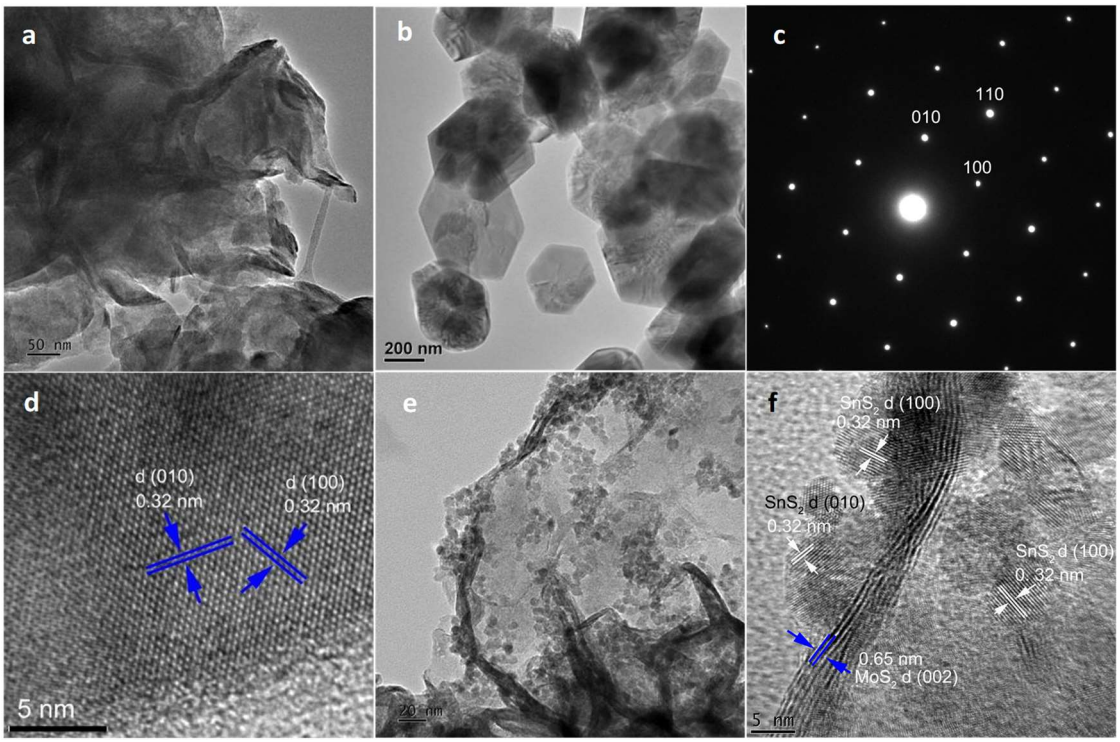

Figure 2. (**a**) TEM image of MoS_2, (**b**) TEM image of SnS_2, (**c**) SAED pattern of SnS_2 on one single crystal, (**d**) HRTEM image of SnS_2, (**e**) TEM image of SnS_2/MoS_2 nanocomposite, (**f**) HRTEM image of SnS_2/MoS_2 nanocomposite.

The chemical state of the as-prepared materials was further investigated by XPS analysis. Figure 3a–c shows the XPS spectra of Sn 3d, Mo 3d and S 2p in different samples. The peak positions of Sn $3d_{3/2}$ and Sn $3d_{5/2}$ in pure SnS_2 are located at 495.2 and 486.7 eV, respectively, while these peaks shift to 495.6 and 487.1 eV, respectively in the SnS_2/MoS_2 nanocomposite. The increased binding energy of Sn 3d in the composite material may be ascribed to the electron transfer from Sn to Mo element in the interface of the SnS_2/MoS_2 nanocomposite. This electron transfer is further confirmed by the change of Mo 3d XPS spectrum. As shown in Figure 3b, the binding energies of Mo $3d_{3/2}$ and Mo $3d_{5/2}$ in pure MoS_2 are 232.17 and 229.08 eV, while these values are shifted to 232.12 and 229.0 eV in the SnS_2/MoS_2 composite. The decreased binding energy of Mo 3d in the SnS_2/MoS_2 composite may be attributed to the electron transfer from Sn to the adjacent Mo element. The shift of the binding energies of Mo 3d and Sn 3d proved the strong chemical interaction between SnS_2 quantum dots and MoS_2 nanosheets in the composite material. There is no obvious differences in the S 2p XPS spectrum (Figure 3c) between MoS_2 and SnS_2. However, both S $2p_{1/2}$ and S $2p_{3/2}$ shifted to higher binding energies in the SnS_2/MoS_2 composite, which further confirmed the strong chemical interactions between S, Sn, and Mo in the SnS_2/MoS_2 composite.

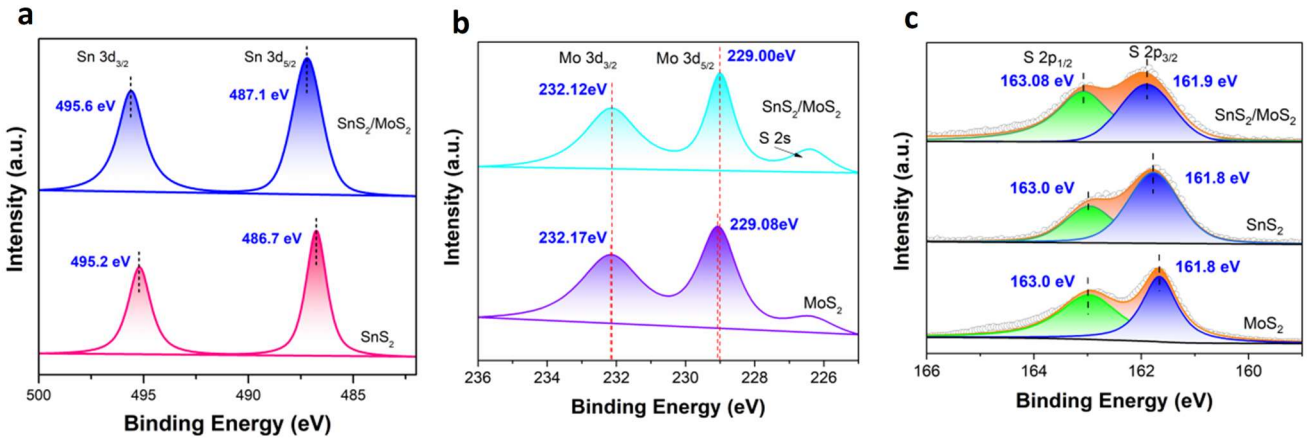

Figure 3. (**a**) Sn 3d XPS spectra of the SnS_2 and SnS_2/MoS_2 samples, (**b**) Mo 3d XPS spectra of the MoS_2 and SnS_2/MoS_2 samples, (**c**) S 2p XPS spectra of SnS_2, MoS_2 and SnS_2/MoS_2 samples.

UV-vis spectroscopy was used to study the optical absorption of the samples. As shown in Figure 4a, all of the samples exhibited visible light absorption property. The SnS_2 sample absorbs light from UV light to visible light with wavelength shorter than 550 nm, while the MoS_2 nanosheets show an intense light absorption from UV light to almost the entire visible light region with an absorption band edge around 700 nm, which is similar to our previous studies [43]. Compared with bare SnS_2 and MoS_2 samples, the SnS_2/MoS_2 nanocomposite showed much increasing light absorption in the visible light region beyond 700 nm, indicating that the composition of SnS_2 and MoS_2 can extend the light absorption capability of photocatalysts. For a crystalline semiconductor, the optical absorption near the band edge follows the equation [48]: $ah\upsilon = A(h\upsilon - E_g)^{n/2}$, where a, υ, A and E_g are the absorption coefficient, light frequency, proportionality constant and band gap, respectively. n depends on whether the transition is direct ($n = 1$) or indirect ($n = 4$). The values of n and E_g were determined by the following steps: at first, plot $\ln(ah\upsilon)$ vs $\ln(h\upsilon - E_g)$, using an approximate value of E_g, and then determine the value of n with the slope of the straightest line near the band edge; second, plot $(ah\upsilon)^{1/n}$ vs $h\upsilon$ and then evaluate the band gap E_g by extrapolating the straightest line to the $h\upsilon$ axis intercept [49]. According to the equation, the value of n is estimated to be 1 or 4 for SnS_2 and MoS_2, respectively. As shown in Figure 4b,c, the band gaps of SnS_2 and MoS_2 are estimated to be about 1.90 and 1.46 eV, respectively.

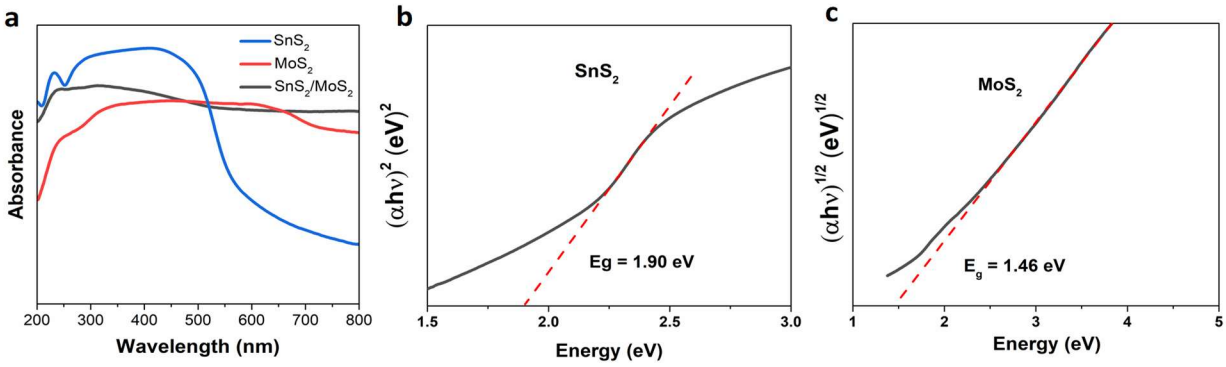

Figure 4. (**a**) Ultraviolet-visible absorption spectra of the different samples, (**b**) *ahv-hv* curve of SnS_2, (**c**) *ahv-hv* curve of MoS_2.

3.2. Photocatalytic Activity

The as-prepared SnS_2/MoS_2 nanocomposite exhibited photocatalytic H_2 evolution performance in CO_2 saturated aqueous solution under 300 W Xenon light irradiation. Blank experiments revealed that there was no H_2 and hydrogenated carbon products before and after light irradiation in the reaction cell without catalyst or light irradiation. Figure 5a–c showed the yields of H_2, CH_4, and CO product on SnS_2/MoS_2, bare SnS_2 and bare MoS_2 catalyst, respectively under light irradiation. It can be seen that the amount of these products increased almost linearly with increasing irradiation time. Although the catalyst was dispersed in CO_2 saturated water, H_2 is the majority product from SnS_2/MoS_2 and pure SnS_2 photocatalyst. Only a small amount of CH_4 and CO products are observed. Compared with SnS_2/MoS_2 and pure SnS_2, the amount of CH_4 and CO are obviously increasing on pure MoS_2 catalyst. The increasing yield of CH_4 in the case of MoS_2 can be attributed to the accumulated electrons from charged excitons on catalyst surface [43], which facilitates muti-electron reduction reactions, such as $CO_2 \rightarrow CH_4$ (8 electron transfer). Correspondingly, the production of H_2 on MoS_2 by the single electron reduction process ($H^+ + e \rightarrow H\cdot$) is much lower than that on SnS_2 as reported [44–46]. According to Figure 5a, the total amounts of H_2, CH_4, and CO generated on SnS_2/MoS_2 catalyst were 915.2, 81.52, and 33.0 μmol/g within 22 h (Figure 5a). Therefore, the selectivity of the photogenerated electrons for H_2, CH_4, and CO generation are 81.1%,

11.7%, and 7.2%, respectively. Under the same condition, the total amount of H_2, CH_4, and CO generated on the SnS_2 catalyst were 463.1, 47.5, and 18.7 μmol/g within 22 h (Figure 5b), corresponding to a selectivity of 68.9%, 28.3%, and 2.8% of the photogenerated electrons for generating H_2, CH_4, and CO, respectively. Figure 5c shows the H_2, CH_4, and CO obtained on the pure MoS_2 during 22-h irradiation in CO_2 saturated water. The total amounts of H_2, CH_4, and CO obtained are 238.2, 170.4, and 63.8 μmol/g, responding to a selectivity of 24.2%, 69.3%, and 6.5% of the photogenerated electrons for H_2, CH_4, and CO production, respectively. Photocatalytic performances of pure MoS_2, pure SnS_2, and SnS_2/MoS_2 nanocomposite indicate that the SnS_2/MoS_2 nanocomposite can increase both the productivity and selectivity of H_2 from CO_2 saturated water under light irradiation. Especially, the amount of H_2 obtained on SnS_2/MoS_2 is almost double of that on SnS_2 within 22 h. The much improved H_2 productivity and selectivity of the SnS_2/MoS_2 composite catalyst may be ascribed to its superior electron-hole separation and faster charge transfer at the interface of an S-scheme heterojunction structure, which will be further discussed in the following sections.

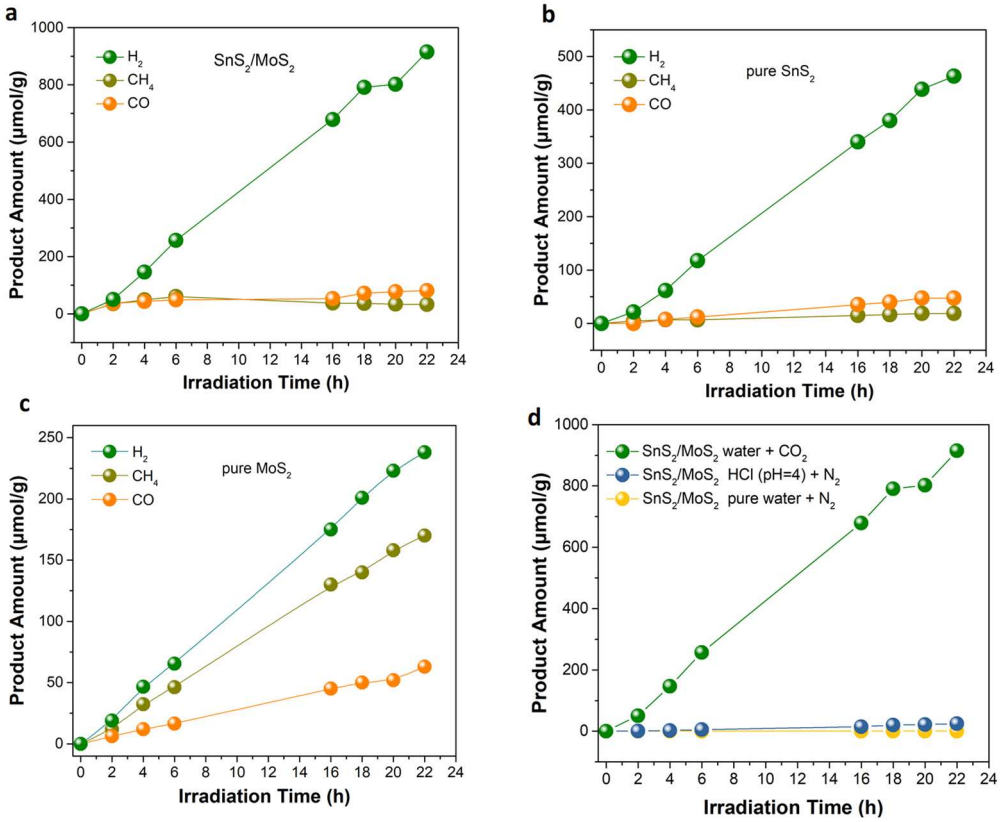

Figure 5. Photocatalytic performances of (**a**) SnS_2/MoS_2, (**b**) pure SnS_2 and (**c**) pure MoS_2 in CO_2 saturated aqueous solution. (**d**) Comparison of photocatalytic H_2 evolution performance of SnS_2/MoS_2 in different reaction mediums.

To investigate the role of CO_2 in H_2 evolution from CO_2 saturated water, comparative experiments were conducted in N_2 saturated pure water and N_2 saturated hydrochloric acid solution (pH 4). As shown in Figure 5d, no H_2 was observed when CO_2 was replaced by N_2 to fill in the reaction cell. Only trace amount of H_2 was obtained in acidic N_2 saturated water. These results revealed that H_2 evolution may come from CO_2 reduction intermediates but not from direct water splitting.

3.3. Photocatalytic Mechanisms

To further understand the much higher performance and the mechanism of hydrogen evolution on SnS_2/MoS_2, an electrochemical analysis was conducted. Figure 6a displays the electrochemical impedance spectroscopy (EIS) of SnS_2, MoS_2 and SnS_2/MoS_2. Compared with other samples, SnS_2/MoS_2 exhibited the minimum arc radius of the impedance spectrum, suggesting the more efficient charge transfer in the heterojunction structure, which could better promote the separation and migration of photoinduced charge carriers [50,51]. Linear sweep voltammetry (LSV) scans were performed to directly determine the over potentials for water reduction by different samples on FTO conducting substrate in 0.1 M Na_2SO_4 solution at pH 7. As shown in Figure 6b, cathodic scans revealed the over potentials for water reduction were located at about −0.37 and −0.3 V vs. NHE for the MoS_2 and SnS_2 samples, respectively. Under the same conditions, the SnS_2/MoS_2 nanocomposite exhibited much lower reduction over potential of about −0.006 V, indicating the much easier water reduction kinetic on SnS_2/MoS_2 nanocomposite. The information on water reduction kinetics of these photocatalysts can be further proved by Tafel plots stemming from the corresponding LSV curves in Figure 6b. As shown in Figure 6c, the Tafel slopes for SnS_2, MoS_2 and SnS_2/MoS_2 samples are 0.3776, 0.4355, and 0.3696 $Vdec^{-1}$, respectively. Lower Tafel slope theoretically indicates faster water reduction kinetics, which facilitates photocatalytic water reduction and CO_2 hydrogenation over the SnS_2/MoS_2 nanocomposite.

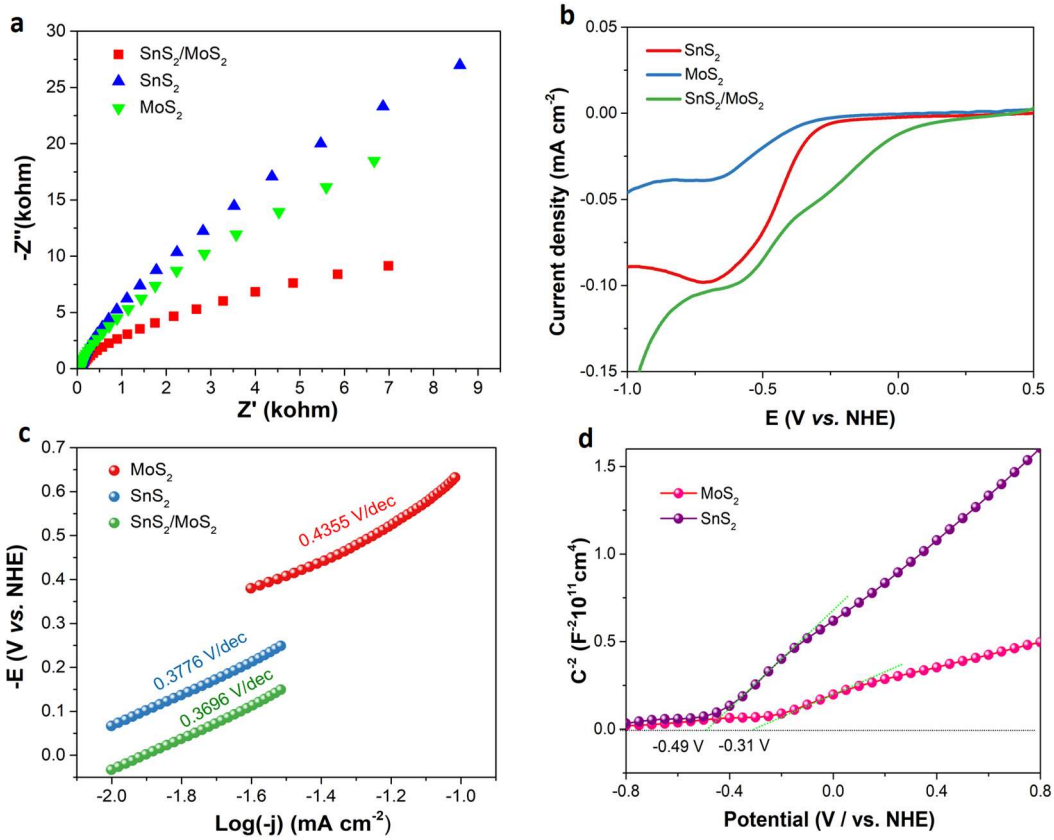

Figure 6. The photo-electrochemical performances of MoS_2, SnS_2 and SnS_2/MoS_2 in 0.1M Na_2SO_4. (**a**) Impedance spectroscopy plots of MoS_2, SnS_2 and SnS_2/MoS_2 under light irradiation, (**b**) Cathodic current-potential scans of different samples in the dark, (**c**) Tafel plots of MoS_2, SnS_2 and SnS_2/MoS_2 obtained from the cathodic current-potential scan, (**d**) Mott-Schottky plots of the synthetic MoS_2 and SnS_2.

The flatband potentials (E_{fb}) of the SnS_2 and MoS_2 electrodes are measured by Mott-Schottky analysis, which was generated from the capacitance values measured at 1000 Hz in dark. As shown in Figure 6d, the positive slopes of the plots indicate the as-prepared SnS_2 and MoS_2 are n-type semiconductor and then electrons are the majority charge carriers. The E_{fb} value was calculated from the intercept of the axis with potential values, which is −0.49 and −0.31 vs. NHE at pH 7 for SnS_2 and MoS_2, respectively. E_{fb} is strongly related to the bottom of the conduction band (E_{cb}) and is usually considered to be about 0.1 V below the E_{cb} for many n-type semiconductors [52]. Therefore, the E_{cb} values for SnS_2 and MoS_2 are estimated as −0.59 and −0.41 vs. NHE at pH 7, respectively. These E_{cb} values enabled the thermodynamic feasibility of the conduction band electrons in SnS_2 and MoS_2 for H^+ reduction to H_2 because the $E(H^+/H_2)$ = −0.41 V at pH 7.

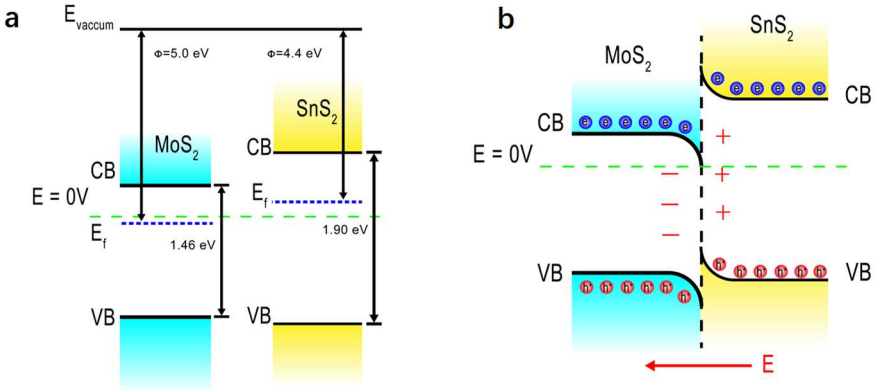

Figure 7. Schematic band energy alignment of SnS_2 and MoS_2 before contacting (**a**) and band bending at the interface (**b**).

According to the band positions calculated from the electrochemical analysis and the work functions of fewer layer MoS_2 and hexagonal SnS_2 [53,54], S-sheme or Type-I heterojunction between MoS_2 and SnS_2 may be formed [8]. However, if Type-I was formed, the photogenerated electrons and holes in MoS_2 and SnS_2 will recombine in the interface and then largely suppress the photocatalytic activity. Therefore, S-scheme heterojunction should be constructed between MoS_2 and SnS_2 based on the photocatalytic performance, as shown in Figure 7. According to the band structures of MoS_2 and SnS_2 (Figure 7a), MoS_2 can be

considered as an oxidative photocatalyst with a lower E_f, and SnS_2 is a reductive photocatalyst with a higher E_f. In this case, when the MoS_2 photocatalyst closely contacted with SnS_2, the electrons in SnS_2 spontaneously flowed to the MoS_2 until their Fermi level are the same. After that, an inner electric field (IEF) at the interface of SnS_2/MoS_2 heterojunction was produced and then impeded the continuous flow of electrons from SnS_2 to MoS_2. Under the impact of such an electric field, the band edge of SnS_2 would bend upward because of losing electrons, and the band edge of MoS_2 would bend downward because of accumulating electrons. Under light irradiation, the photogenerated electrons in the CB of MoS_2 will combine with the photogenerated holes in the VB of SnS_2 owing to inner electric field, leaving the powerful CB electrons of SnS_2 and VB holes of MoS_2 in the composite photocatalyst (Figure 7b). As mentioned above, the E_{cb} of SnS_2 QDs and MoS_2 nanosheet were estimated to be about −0.59 and −0.41 vs. NHE at pH 7, respectively. A higher E_{cb} facilitates a faster hydrogen evolution process. Therefore, a S-scheme heterojunction formed in the interface of SnS_2/MoS_2 not only effectively separated the photogenerated electron-hole pairs, but also provided maximized redox ability of the photogenerated charge carriers, responsible for the more efficient hydrogen evolution performance of SnS_2/MoS_2.

3.4. Photocatalytic Reaction Pathways

To further investigate the mechanism of hydrogen evolution in CO_2 saturated solution under light irradiation, DRIFTS was employed to monitor the surface reaction intermediates. Before introducing CO_2, we analyzed the DRIFT spectrum in vacuum in the dark (Figure 8a). Surfaces of the as-prepared MoS_2, SnS_2, and SnS_2/MoS_2 samples were dominated by strongly adsorbed H_2O and CO_2 even in the vacuum state. The absorption band around 1617 and 3300 cm^{-1} were ascribed to bending vibration of H_2O and stretching vibration of –OH [55], respectively, as shown in Figure 8a. Additionally, the distinct peak of 666 and 2359 cm^{-1} were ascribed to bending vibration and asymmetrical stretching vibration of CO_2, respectively [56]. Additionally, the absorption band appeared around 1456 and 1650 cm^{-1} were attributed to symmetrical and asymmetrical OCO stretching vibration in $HOCOO^-$ (HCO_3^-) species [56]. The absorption bands from bidentate or monodentate carbonate ($–CO_3^{2-}$) species appeared around 1561 cm^{-1} [43]. Unsaturated C–H bond absorption at 2847 and 2922 cm^{-1} may be come from the S–C–H on the surface of catalysts, which come from surface organic contaminant during the sample preparation [43]. A weak absorbance around 2514 cm^{-1} was assigned to stretching vibration of S–H [43].

In situ DRIFT spectra were recorded after introducing CO_2 and H_2O to further study CO_2 reduction mechanism under light irradiation. Figure 8b showed the change of surface functional groups on pure MoS_2 within different irradiation time. Along with the increased irradiation time, six positive absorption bands emerged around 1065, 1285, 1358, 1528, 1783, and 2497 cm^{-1}, which were ascribed to the stretching vibration of C–O bond in –HC–OH [43], the stretching vibration of C–O bond in –COOH group [43], the stretching vibration of C–O bond in HCOO– [57], the stretching vibration of C=O bond in HCOO– [57], the stretching vibration of C=O bond in –COOH [43] and the surface S–H group, respectively. Simultaneously, four negative absorption peaks appeared at 1439, 1608, 1671 and 3400 cm^{-1}, indicating the decreasing concentrations of the surface HCO_3^- and H_2O species, respectively. The change of the absorption bands in DRIFT spectra revealed the reaction of HCO_3^- and H_2O to generate –HC–OH, –COOH, HCOO–, and –H species under light irradiation on the surface of pure MoS_2. H_2 evolution during the CO_2 hydrogenation process may be mainly ascribed to the decomposition of these hydrogenated intermediates and the release of H radicals from –H under light irradiation.

The in situ DRIFT spectra on SnS_2 under the same condition are shown in Figure 8c. Similar to the pure MoS_2, the absorption bands from HCO_3^- (1420 and 1656 cm^{-1}) and H_2O (1602 and 3239 cm^{-1}) are gradually decreased along with the light irradiation increasing time. By contrast, six positive absorption bands emerged around 1112, 1288, 1347, 1523, 1794, and 2500 cm^{-1}, which are ascribed to the stretching vibration of C–O bond in –HC–OH, the stretching vibration of C–O bond in –COOH, the stretching vibration of C–O in HCOO–, the stretching vibration of C=O bond in HCOO–, the stretching vibration of C=O bond in –COOH and the surface S–H group, respectively. This suggested that HCO_3^- and H_2O react with each other to generate –HC–OH, –COOH, HCOO– and –H intermediates on the SnS_2 surface, similar to that on MoS_2. However, there are some differences on the in situ DRIFT spectrum between MoS_2 and SnS_2 for CO_2 reduction. First of all, the absorption intensity from S–H group in SnS_2 is obviously larger than that in MoS_2 under the same condition. The better H_2 evolution performance of SnS_2 may partially originate from the higher dissociation of H from S–H.

DRIFT spectra in Figure 8d revealed the CO_2 hydrogenation process on SnS_2/MoS_2. Under light irradiation, the absorption bands from HCO_3^- (1435 and 1635 cm^{-1}) and surface –OH (3353 cm^{-1}) are dramatically decreased along with the obviously increasing absorption bands from –COOH and HCOO– species, indicating the reaction of surface HCO_3^- and –OH to generate –HC–OH, –COOH and HCOO– intermediates. Different from MoS_2 and SnS_2, it was found the absorption band from the surface S–H group did not emerge after light irradiation on SnS_2/MoS_2. The reasons for the disappearance of the S–H absorption band on SnS_2/MoS_2 may be ascribed to the faster reaction kinetics in S-scheme structure for H radials release from S–H species once they are formed on the surface. Furthermore, it was found the absorption bands from –COOH species on SnS_2/MoS_2 are broader and stronger compared with that on bare MoS_2 and SnS_2, indicating the diversity of the reactive sites for –COOH generation. Considering the appearance of –HC–OH, –COOH and HCOO– species on the three samples and their increasing concentrations under light irradiation, H_2 evolution may partly arise from the decomposition of these carbon-hydrogen species. Both the enhanced

concentrations of carbon-hydrogen intermediate species and the faster dissociation of H from S–H on the SnS_2/MoS_2 surface may be responsible for the higher H_2 evolution performance.

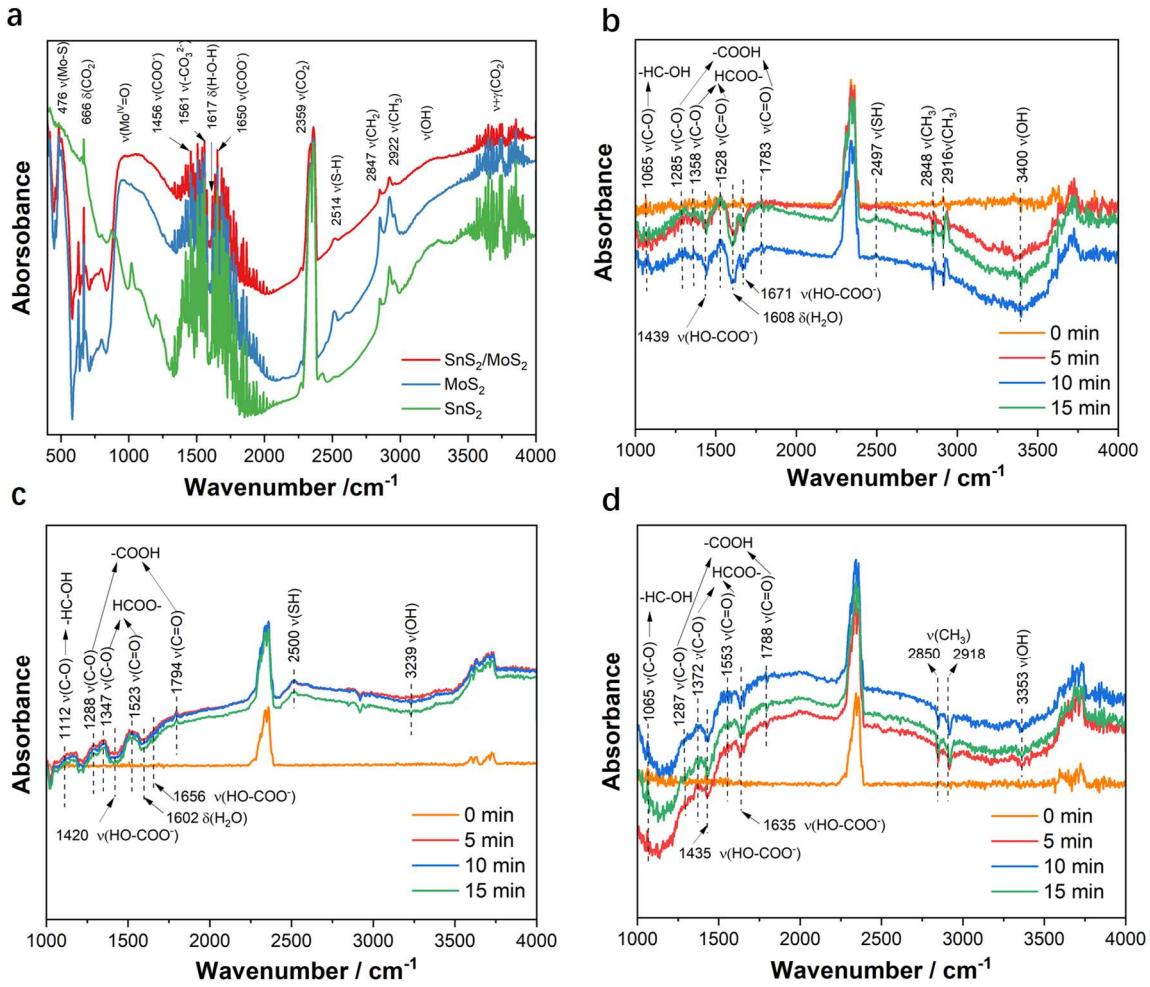

Figure 8. CO_2 adsorption and activation on different samples revealed by *in-situ* DRIFT observation. (**a**) DRIFT spectra of different samples under vacuum in the dark. b, c, d. *In situ* DRIFT spectra recorded after ambient temperature adsorption of CO_2/H_2O on pure MoS_2 (**b**), pure SnS_2 (**c**) and SnS_2/MoS_2 (**d**) under 300 W Xe arc lamp irradiation.

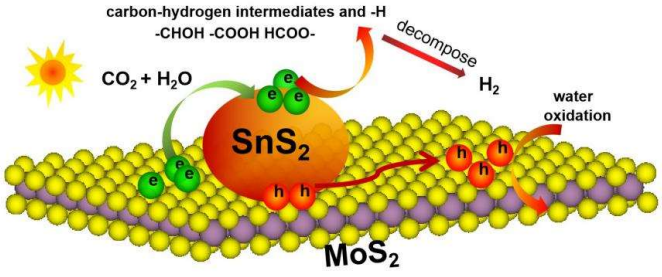

Figure 9. Schematic illustration of H_2 generation process in CO_2 saturated solution on SnS_2/MoS_2 catalyst.

The phenomena observed from in situ DRIFT spectra on MoS_2, SnS_2, and SnS_2/MoS_2 confirmed the reasons for the better photocatalytic activity of the SnS_2/MoS_2 nanocomposite. The whole H_2 generation process on SnS_2/MoS_2 is illustrated in Figure 9. Under light irradiation, CO_2 is reduced in water by photogenerated electrons to generate carbon-hydrogen intermediates such as –HC–OH, –COOH and HCOO– species, as well as –H species on the surface. Most of these intermediates are not stable, and their decomposition generates H_2 under light irradiation. Furthermore, S-scheme structure decreased the electron-hole recombination and increased the redox ability of the photogenerated charge carriers for both CO_2 reduction and H_2O oxidation, respectively. All of the above reasons endowed the higher efficiency of H_2 evolution by use of SnS_2/MoS_2 in CO_2 saturated solution.

4. Conclusions

0D/2D S-scheme SnS_2/MoS_2 heterojunction nanocomposite was successfully prepared. It permitted a more efficient photocatalytic hydrogen evolution in CO_2 saturated solution. This improved photocatalytic activity was attributed to the S-scheme heterojunction between SnS_2 and MoS_2, which facilitates the electron-hole separation and increases the redox ability of the photogenerated charge carriers. Under the conditions we used, the optimized SnS_2/MoS_2 showed a 1.92- and 3.8-fold enhancement for H_2 evolution when compared with the bare MoS_2 and SnS_2, respectively. This work is thought to significantly boost the development of S-scheme heterojunction photocatalysts for solar energy conversion.

Author Contributions

Conceptualization, S.S.; Methodology, X.C., X.L. and L.L.; Validation, X.L.; Formal Analysis, X.C., X.L. and L.L.; Investigation, X.C. and X.L.; Resources, S.S. and X.C.; Writing-Original Draft Preparation, X.C. and X.L.; Writing-Review & Editing, S.S., X.C., J.P. and X.L.; Supervision, S.S.; Project Administration, S.S.; Funding Acquisition, S.S.

Acknowledgements

This work was financially supported by Natural Science Foundation of Shanghai (No. 21ZR1401600).

Ethics Statement

Not applicable.

Informed Consent Statement

Not applicable.

Declaration of Competing Interest

The authors declare that they have no known competing financial interests or personal relationships that could have appeared to influence the work reported in this paper.

References

1. Chen B, Meng Y, Sha J, Zhong C, Hu W, Zhao N. Preparation of MoS_2/TiO_2 based nanocomposites for photocatalysis and rechargeable batteries: progress, challenges, and perspective. *Nanoscale* **2017**, *10*, 34–68.
2. Lin Y, Liu X, Liu Z, Xu Y. Visible-Light-Driven Photocatalysis-Enhanced Nanozyme of TiO_2 Nanotubes@MoS_2 Nanoflowers for Efficient Wound Healing Infected with Multidrug-Resistant Bacteria. *Small* **2021**, *17*, e2103348.
3. Ye K, Li Y, Yang H, Li M, Huang Y, Zhang S, Ji H. An ultrathin carbon layer activated CeO_2 heterojunction nanorods for photocatalytic degradation of organic pollutants. *Appl. Catal. B Environ.* **2019**, *259*, 118085.
4. Chava RK, Do JY, Kang M. Enhanced photoexcited carrier separation in CdS–SnS_2 heteronanostructures: a new 1D–0D visible-light photocatalytic system for the hydrogen evolution reaction. *J. Mater. Chem. A* **2019**, *7*, 13614–13628.
5. Xu Q, Ma D, Yang S, Tian Z, Cheng B, Fan J. Novel g-C_3N_4/g-C_3N_4 S-scheme isotype heterojunction for improved photocatalytic hydrogen generation. *Appl. Surf. Sci.* **2019**, *495*, 143555.
6. Low J, Jiang C, Cheng B, Wageh S, Al-Ghamdi AA, Yu J. A Review of Direct Z-Scheme Photocatalysts. *Small Methods* **2017**, *1*, 1700080.
7. Li J, Li M, Jin Z. Rational design of a cobalt sulfide/bismuth sulfide S-scheme heterojunction for efficient photocatalytic hydrogen evolution. *J. Colloid Interf. Sci*. **2021**, *592*, 237–248.
8. Xu Q, Zhang L, Cheng B, Fan J, Yu J. S-scheme heterojunction photocatalyst. *Chem* **2020**, *6*, 1543–1559.
9. Jiang Y, Sun Z, Chen Q, Cao C, Zhao Y, Yang W, et al. Fabrication of 0D/2D TiO_2 Nanodots/g-C_3N_4 S-scheme heterojunction photocatalyst for efficient photocatalytic overall water splitting. *Appl. Surf. Sci.* **2022**, *571*, 151287.
10. Bai J, Shen R, Chen W, Xie J, Zhang P, Jiang Z, et al. Enhanced photocatalytic H_2 evolution based on a $Ti_3C_2/Zn_{0.7}Cd_{0.3}S/Fe_2O_3$ Ohmic/S-scheme hybrid heterojunction with cascade 2D coupling interfaces. *Chem. Eng. J.* **2022**, *429*, 132587.
11. Li B, Zhang B, Zhang Y, Zhang M, Huang W, Yu C, et al. Prediction of the failure probability of the overhead power line exposed to large-scale jet fires induced by high-pressure gas leakage. *Int. J. Hydrogen Energ.* **2021**, *46*, 2413–2431.
12. Liu T, Yang K, Gong H, Jin Z. Visible-light driven S-scheme $Mn_{0.2}Cd_{0.8}S/CoTiO_3$ heterojunction for photocatalytic hydrogen evolution. *Renew. Energ.* **2021**, *173*, 389–400.
13. Xu X, Su Y, Dong Y, Luo X, Wang S, Zhou W, et al. Designing and fabricating a CdS QDs/Bi_2MoO_6 monolayer S-scheme heterojunction for highly efficient photocatalytic C_2H_4 degradation under visible light. *J. Hazard. Mater.* **2022**, *424*, 127685.
14. Wu S, Yu X, Zhang J, Zhang Y, Zhu Y, Zhu M. Construction of BiOCl/$CuBi_2O_4$ S-scheme heterojunction with oxygen vacancy for enhanced photocatalytic diclofenac degradation and nitric oxide removal. *Chem. Eng. J.* **2021**, *411,* 128555.
15. Sabzehparvar M, Kiani F, Tabrizi NS. Mesoporous-assembled TiO_2-NiO-Ag nanocomposites with pn/Schottky heterojunctions for enhanced

photocatalytic performance. *J. Alloy. Compd.* **2021**, *876,* 160133.
16. Liu J, Wei X, Sun W, Guan X, Zheng X, Li J. Fabrication of S-scheme CdS-g-C_3N_4-graphene aerogel heterojunction for enhanced visible light driven photocatalysis. *Environ. Res.* **2021**, *197*, 111136.
17. Wang A, Ni J, Wang W, Wang X, Liu D, Zhu Q. MOF-derived N-doped ZnO carbon skeleton@hierarchical Bi_2MoO_6 S-scheme heterojunction for photodegradation of SMX: Mechanism, pathways and DFT calculation. *J. Hazard Mater.* **2022**, *426,* 128106.
18. Van Pham V, Mai DQ, Bui DP, Van MT, Zhu B, Zhang L, et al. Emerging 2D/0D g-C_3N_4/SnO_2 S-scheme photocatalyst: new generation architectural structure of heterojunctions toward visible-light-driven NO degradation. *Environ. Pollut.* **2021**, *286*, 117510.
19. Dong Z, Zhang Z, Jiang Y, Chu Y, Xu J. Embedding $CsPbBr_3$ perovskite quantum dots into mesoporous TiO_2 beads as an S-scheme heterojunction for CO_2 photoreduction. *Chem. Eng. J.* **2022**, *433,* 133762.
20. Wang Z, Cheng B, Zhang L, Yu J, Tan H. BiOBr/NiO S-Scheme Heterojunction Photocatalyst for CO_2 Photoreduction. *Solar RRL* **2021**, *6*, 2100587.
21. Yu B, Wu Y, Meng F, Wang Q, Jia X, Wasim Khan M, et al. Formation of hierarchical Bi_2MoO_6/ln_2S_3 S-scheme heterojunction with rich oxygen vacancies for boosting photocatalytic CO_2 reduction. *Chem. Eng. J.* **2022**, *429,* 132456.
22. Liu L, Dai K, Zhang J, Li L. Plasmonic Bi-enhanced ammoniated α-MnS/Bi_2MoO_6 S-scheme heterostructure for visible-light-driven CO_2 reduction. *J. Colloid Interf. Sci.* **2021**, *604*, 844–855.
23. Wang J, Yu Y, Cui J, Li X, Zhang Y, Wang C, et al. Defective g-C_3N_4/covalent organic framework van der Waals heterojunction toward highly efficient S-scheme CO_2 photoreduction. *Appl. Catal. B Environ.* **2022**, *301,* 120814.
24. Chen Q, Lan X, Chen K, Ren Q, Shi J. Construction of WO_3/$CsPbBr_3$ S-scheme heterojunction via electrostatic Self-assembly for efficient and Long-Period photocatalytic CO_2 reduction. *J. Colloid Interf. Sci.* **2022**, *616*, 253–260.
25. Wang L, Cheng B, Zhang L, Yu J. In situ Irradiated XPS Investigation on S-Scheme TiO_2@$ZnIn_2S_4$ Photocatalyst for Efficient Photocatalytic CO_2 Reduction. *Small* **2021**, *17*, e2103447.
26. Gong S, Teng X, Niu Y, Liu X, Xu M, Xu C, et al. Construction of S-scheme 0D/2D heterostructures for enhanced visible-light-driven CO_2 reduction. *Appl. Catal. B Environ.* **2021**, *298,* 120521.
27. Zhang Z, Cao Y, Zhan F, Li W, Li Y, Yu H, et al. Tungsten oxide quantum dots deposited onto ultrathin $CdIn_2S_4$ nanosheets for efficient S-scheme photocatalytic CO_2 reduction via cascade charge transfer. *Chem. Eng. J.* **2022**, *428,* 131218.
28. Deng H, Fei X, Yang Y, Fa J, Yu J, Cheng B, et al. S-scheme heterojunction based on p-type $ZnMn_2O_4$ and n-type ZnO with improved photocatalytic CO_2 reduction activity. *Chem. Eng. J.* **2021**, *409,* 127377.
29. Xia P, Cao S, Zhu B, Liu M, Shi M, Yu J, et al. Designing a 0D/2D S-scheme heterojunction over polymeric carbon nitride for visible-light photocatalytic inactivation of bacteria. *Angew. Chem. Int. Ed.* **2020**, *59*, 5218–5225.
30. Aihemaiti X, Wang X, Li Y, Wang Y, Xiao L, Ma Y, et al. Enhanced photocatalytic and antibacterial activities of S-scheme SnO_2/Red phosphorus photocatalyst under visible light. *Chemosphere* **2022**, *296,* 134013.
31. Liu J, Huang L, Li Y, Yao J, Shu S, Huang L, et al. Constructing an S-scheme $CuBi_2O_4$/$Bi_4O_5I_2$ heterojunction for light emitting diode-driven pollutant degradation and bacterial inactivation. *J. Colloid Interf. Sci.* **2022**, *621,* 295–310.
32. Yang H, He D, Liu C, Zhang T, Qu J, Jin D, et al. Visible-light-driven photocatalytic disinfection by S-scheme α-Fe_2O_3/g-C_3N_4 heterojunction: Bactericidal performance and mechanism insight. *Chemosphere* **2022**, *287*, 132072.
33. Kang Y, Gong Y, Hu Z, Li Z, Qiu Z, Zhu X, et al. Plasmonic hot electron enhanced MoS_2 photocatalysis in hydrogen evolution. *Nanoscale* **2015**, *7*, 4482–4488.
34. Maitra U, Gupta U, De M, Datta R, Govindaraj A, Rao CN. Highly effective visible-light-induced H_2 generation by single-layer 1T-MoS_2 and a nanocomposite of few-layer 2H-MoS (2) with heavily nitrogenated graphene. *Angew. Chem. Int. Ed.* **2013**, *52*, 13057–13061.
35. Singh N, Jabbour G, Schwingenschlögl U. Optical and photocatalytic properties of two-dimensional MoS_2. *Eur. Phys. J. B* **2012**, *85*, 1–4.
36. Yuan YJ, Lu HW, Yu ZT, Zou ZG. Noble-metal-free molybdenum disulfide cocatalyst for photocatalytic hydrogen production. *ChemSusChem* **2015**, *8*, 4113–4127.
37. Huo Y, Yang Y, Dai K, Zhang J. Construction of 2D/2D porous graphitic C_3N_4/SnS_2 composite as a direct Z-scheme system for efficient visible photocatalytic activity. *Appl. Surf. Sci.* **2019**, *481*, 1260–1269.
38. Zhang YC, Yao L, Zhang G, Dionysiou DD, Li J, Du X. One-step hydrothermal synthesis of high-performance visible-light-driven SnS_2/SnO_2 nanoheterojunction photocatalyst for the reduction of aqueous Cr(VI). *Appl. Catal. B Environ.* **2014**, *144*, 730–738.
39. Zhang Z, Huang J, Zhang M, Yuan Q, Dong B. Ultrathin hexagonal SnS_2 nanosheets coupled with g-C_3N_4 nanosheets as 2D/2D heterojunction photocatalysts toward high photocatalytic activity. *Appl. Catal. B Environ.* **2015**, *163*, 298–305.
40. Yin S, Li J, Sun L, Li X, Shen D, Song X, et al. Construction of Heterogenous S–C–S MoS_2/SnS_2/r-GO Heterojunction for Efficient CO_2 Photoreduction. *Inorg. Chem.* **2019**, *58*, 15590–15601.
41. Zhang J, Huang G, Zeng J, Jiang X, Shi Y, Lin S, et al. SnS_2 nanosheets coupled with 2D ultrathin MoS_2 nanolayers as face-to-face 2D/2D heterojunction photocatalysts with excellent photocatalytic and photoelectrochemical activities. *J. Alloy. Compd.* **2019**, *775*, 726–735.
42. Dong R, Zhong Y, Chen D, Li N, Xu Q, Li H, et al. Morphology-controlled fabrication of CNT@ MoS_2/SnS_2 nanotubes for promoting photocatalytic reduction of aqueous Cr (VI) under visible light. *J. Alloy. Compd.* **2019**, *784*, 282–292.
43. Sun S, An Q, Watanabe M, Cheng J, Kim HH, Akbay T, et al. Highly correlation of CO_2 reduction selectivity and surface electron Accumulation: A case study of Au-MoS_2 and Ag-MoS_2 catalyst. *Appl. Catal. B Environ.* **2020**, *271*, 118931.

44. Hu L, Song XF, Zhang SL, Zeng HB, Zhang XJ, Marks R, et al. MoS_2 nanoparticles coupled to SnS_2 nanosheets: The structural and electronic modulation for synergetic electrocatalytic hydrogen evolution. *J. Catal.* **2018**, *366,* 8–15.
45. Xiao X, Wang Y, Xu X, Yang T, Zhang D. Preparation of the flower-like MoS_2/SnS_2 heterojunction as an efficient electrocatalyst for hydrogen evolution reaction. *Mol. Catal.* **2020**, *487*, 110890.
46. Mangiri R, Subramanyam K, Ratnakaram Y, Sudharani A, Reddy DA, Vijayalakshmi R. Boosting solar driven hydrogen evolution rate of CdS nanorods adorned with MoS_2 and SnS_2 nanostructures. *Colloid Interf. Sci.* **2021**, *43*, 100437.
47. Sun S, Wang W, Li D, Zhang L, Jiang D. Solar Light Driven Pure Water Splitting on Quantum Sized $BiVO_4$ without any Cocatalyst. *ACS. Catal.* **2014**, *4*, 3498–3503.
48. Butler M. Photoelectrolysis and physical properties of the semiconducting electrode WO_2. *J. Appl. Phys.* **1977**, *48*, 1914–1920.
49. Sun S, Wang W, Zhang L, Zhou L, Yin W, Shang M. Visible Light-Induced Efficient Contaminant Removal by Bi_5O_7I. *Environ. Sci. Technol.* **2009***, 43,* 2005–2010.
50. Su B, Huang H, Ding Z, Roeffaers MB, Wang S, Long J. S-scheme $CoTiO_3/Cd_{9.51}Zn_{0.49}S_{10}$ heterostructures for visible-light driven photocatalytic CO_2 reduction. *J. Mater. Sci. Technol.* **2022**, *124*, 164–170.
51. Li B, Wang W, Zhao J, Wang Z, Su B, Hou Y, et al. All-solid-state direct Z-scheme $NiTiO_3/Cd_{0.5}Zn_{0.5}S$ heterostructures for photocatalytic hydrogen evolution with visible light. *J. Mater. Chem. A* **2021**, *9*, 10270–10276.
52. Ishikawa A, Takata T, Kondo JN, Hara M, Kobayashi H, Domen K. Oxysulfide $Sm_2Ti_2S_2O_5$ as a Stable Photocatalyst for Water Oxidation and Reduction under Visible Light Irradiation ($\lambda \leq 650$ nm). *J. Am. Chem. Soc.* **2002**, *124*, 13547–13553.
53. Tamulewicz M, Kutrowska-Girzycka J, Gajewski K, Serafinczuk J, Sierakowski A, Jadczak J, et al. Layer number dependence of the work function and optical properties of single and few layers MoS_2: effect of substrate. *Nanotechnology* **2019**, *30*, 245708.
54. Ham G, Shin S, Park J, Choi H, Kim J, Lee YA, et al. Tuning the electronic structure of tin sulfides grown by atomic layer deposition. *ACS Appl. Mater. Interf.* **2013**, *5*, 8889–8896.
55. Vasylieva A, Doroshenko I, Vaskivskyi Y, Chernolevska Y, Pogorelov V. FTIR study of condensed water structure. *J. Mol. Struct.* **2018**, *1167*, 232–238.
56. Sun S, Watanabe M, Wu J, An Q, Ishihara T. Ultrathin $WO_3 \cdot 0.33H_2O$ Nanotubes for CO_2 Photoreduction to Acetate with High Selectivity. *J. Am. Chem. Soc.* **2018**, *140*, 6474–6482.
57. Figueiredo MC, Ledezma-Yanez I, Koper MT. In Situ Spectroscopic Study of CO_2 Electroreduction at Copper Electrodes in Acetonitrile. *ACS Catal.* **2016**, *6,* 2382–2392.